MDPI

Article

Optical Properties of Yttrium Ferrite Films Prepared by Pulse Laser Deposition

Dinara Sobola [1,*], Saleh H. Fawaeer [2], Pavla Kočková [2], Richard Schubert [2], Rashid Dallaev [2] and Tomáš Trčka [2]

1 Institute of Physics of Materials, Czech Academy of Sciences, Žižkova 22, 61662 Brno, Czech Republic
2 Department of Physics, Faculty of Electrical Engineering and Communication, Brno University of Technology, Technická 2848/8, 61600 Brno, Czech Republic; saleh.hekmat@ceitec.vutbr.cz (S.H.F.); xsneubauerovap@vut.cz (P.K.); xschub01@vut.cz (R.S.); xdalla03@vut.cz (R.D.); trcka@vut.cz (T.T.)
* Correspondence: sobola@ipm.cz

Abstract: This study investigates the optical properties of yttrium ferrite thin films fabricated via pulse laser deposition. Yttrium orthoferrite, a ferrimagnetic material known for its potential applications in spintronics and photonics, was deposited on single-crystal substrates under controlled conditions to analyze its optical characteristics. The influence of deposition time on the film quality and optical properties was examined. Atomic force microscopy in contact mode revealed surface roughness variations up to 35 nm, indicating the films' ability to cover substrate defects. Reflectance measurements determined the optical band gap, which decreased from 3.17 eV for thinner films (44 nm) to 2.91 eV for thicker films (93 nm). Forbidden electronic transitions were also observed, attributed to heteroepitaxial growth and phonon interactions. These results demonstrate the effect of film thickness on morphology and optical properties, making $YFeO_3$ films promising for a range of optoelectronic applications.

Keywords: yttrium orthoferrite; plasma laser deposition; optical properties; thin films; bandgap; optoelectronics

1. Introduction

Yttrium ferrite ($YFeO_3$, YFO thin films have garnered significant attention in the scientific community due to their unique and valuable properties. Yttrium ferrite thin films exhibit excellent magnetic properties, including high coercivity and remanence, making them suitable for various magnetic applications [1]. These films can be engineered to have specific magnetic characteristics, useful in magnetic storage devices, spintronics, and magnetic sensors [2]. Yttrium ferrite belongs to the class of multiferroic materials, which exhibit more than one ferroic order parameter (ferromagnetism, ferroelectricity, or ferroelasticity) simultaneously [3]. This dual functionality is highly beneficial for advanced electronic devices, allowing for the development of components that can be controlled by both electric and magnetic fields [4]. In microelectronics, yttrium ferrite thin films are used for their dielectric properties. Their high dielectric constant and low loss tangent make them suitable for capacitors and other electronic components where minimizing energy loss is crucial [5]. Yttrium ferrite thin films are also explored for energy storage and conversion applications [6]. Their ability to maintain stable performance under varying environmental conditions is advantageous for batteries, supercapacitors, and fuel cells [7]. The chemical stability of yttrium ferrite thin films is another important characteristic, making them suitable for harsh environments where other materials might degrade [8]. This stability is beneficial for coatings, sensors, and other applications requiring long-term reliability [9].

The optical properties of yttrium ferrite thin films, such as their band gap and refractive index, can be tailored through thin film fabrication techniques. This tunability makes them

suitable for optoelectronic applications, including photodetectors, photovoltaics, and light-emitting devices [10,11]. One of the primary optical properties of yttrium ferrite thin films is their band gap. The band gap of YFO is a critical parameter that defines its electronic and optical behavior. Typically, the band gap of yttrium ferrite thin films is in the range of 2.0 to 2.2 eV. This makes them suitable for applications in visible light photodetection and photovoltaic devices. The direct band gap facilitates efficient electron transition from the valence band to the conduction band upon light absorption, making YFO thin films efficient light absorbers. Allowed direct transition refers to a transition where an electron can directly move from the valence band to the conduction band without a change in momentum. These transitions are allowed by quantum mechanical selection rules, meaning they have a high probability of occurring and typically occur in direct bandgap materials. Forbidden direct transitions occur in cases where direct transitions between the valence and conduction bands are theoretically forbidden by selection rules but can still occur with a lower probability due to perturbations such as lattice defects or impurities. In an allowed indirect transition, an electron moves from the valence band to the conduction band with a change in momentum. This transition requires the involvement of a phonon to conserve momentum. Indirect bandgap materials exhibit this type of transition. Similar to forbidden direct transitions, forbidden indirect transitions occur when the transition between the valence and conduction bands is disallowed by quantum mechanical selection rules but still happens with a lower probability due to defects or other perturbations. These transitions also involve phonons to conserve momentum.

The refractive index (n) of yttrium ferrite thin films is another crucial optical parameter. It typically ranges from 2.2 to 2.6 at visible wavelengths. This high refractive index indicates strong interaction with visible light, which is advantageous for applications in optical coatings and waveguides. The dielectric function, which encompasses both the real (ε1) and imaginary (ε2) parts of the dielectric constant, provides further insights into the material's optical response. The real part of the dielectric function relates to the material's ability to store electrical energy, while the imaginary part corresponds to energy dissipation. For yttrium ferrite, ε1 generally shows a value around 5–6 in the visible range, while ε2 can vary depending on the specific wavelength and film-processing conditions [12].

Yttrium ferrite thin films also exhibit notable optical conductivity. Optical conductivity is a measure of a material's ability to conduct electric current under the influence of an optical field. For YFO thin films, the optical conductivity can be significant in the visible region, contributing to their potential use in optoelectronic devices [13]. Despite their ability to absorb and conduct light, these films maintain a degree of transparency, particularly in the near-infrared region, which is beneficial for applications requiring both conductivity and transparency, such as in transparent electrodes for display technologies [14].

Photoluminescence (PL) is another critical optical property of yttrium ferrite thin films. Under excitation, these films can exhibit strong photoluminescence, typically peaking in the visible spectrum. The PL intensity and peak position can be influenced by factors such as film thickness, crystallinity, and the presence of defects or impurities. This property is particularly valuable for applications in light-emitting devices and sensors. Additionally, yttrium ferrite thin films possess nonlinear optical properties, which are essential for applications in advanced photonic devices [15]. Nonlinear optical behavior such as second-harmonic generation has been observed in these films, indicating their potential in frequency-doubling applications and in the development of photonic circuits [16].

The optical properties of yttrium ferrite thin films can be finely tuned through various doping strategies and fabrication techniques [10]. For instance, doping with elements such as titanium (Ti) or cobalt (Co) can modify the band gap, refractive index, and photoluminescence characteristics. Advanced fabrication techniques such as pulsed laser deposition (PLD), sputtering, and sol–gel methods allow precise control over film thickness, crystallinity, and surface morphology, further influencing the optical properties [12]. For example, PLD can produce highly crystalline films with smooth surfaces, which are crucial for minimizing scattering losses in optical applications [17].

While the current literature on YFO thin films has provided significant insights into their optical properties and potential applications in spintronics and photonics, several critical gaps remain that hinder a comprehensive understanding and broader application of these materials. Existing studies often lack a detailed characterization of the full spectrum of optical properties. Specific measurements of the band gap, absorption coefficients, refractive index, and dielectric constants across a range of wavelengths are not consistently reported. These incomplete data hamper the ability to tailor these materials for precise optoelectronic applications. The literature frequently mentions the fabrication of YFO thin films using various deposition techniques such as plasma laser deposition, sputtering, and sol–gel methods. However, systematic studies on how different deposition parameters—such as substrate temperature, ambient pressure, and laser energy—affect the structural and optical properties of the films are scarce. Understanding these relationships is crucial for optimizing the fabrication process.

This paper systematically examines the influence of deposition time on the quality and optical properties of thin films. This aspect is particularly novel as it provides detailed insights into how varying the deposition duration can affect the topography, composition, and optical performance of the films. Such a systematic study helps in optimizing deposition parameters to achieve the desired film characteristics, which is critical for both fundamental research and practical applications. The pioneering data and interdisciplinary approach presented in this study make it a significant addition to the field of coating technology and materials science. The paper suggests that the optimized deposition conditions can lead to YFO thin films with superior optical properties. This potential for enhanced material performance opens new avenues for the practical use of these films in advanced optoelectronic devices, offering significant improvements over existing materials.

2. Materials and Methods

Yttrium orthoferrite thin films with different thicknesses were deposited on cleaned silicon (Si) substrates (525 ± 25 μm thick). The deposition process was carried out at a temperature of 723.15 K using a pulsed laser deposition system (TSST, Strasbourg, France), with a sintered ceramic pellet of the orthorhombic YFO serving as the PLD target. Prior to deposition, the Si substrates (5 mm × 5 mm) underwent a thorough cleaning procedure. They were initially immersed in a hydrofluoric acid (HF) solution for a duration of 10 min. Subsequently, the substrates were sequentially immersed in high-purity ethanol and distilled water for 10 min each. These meticulously cleaned substrates were then rinsed extensively with distilled water and stored until further use. Just before the film deposition, the Si substrates were thoroughly dried under nitrogen gas. Afterwards, for the depositions, the fabrication of YFO thin films on Si substrates was carried out using a KrF excimer laser with a wavelength of 248 nm. The deposition was performed at a laser energy density of 2 J/cm^2 and a repetition rate of 5 Hz. Throughout the deposition process, the substrate temperature was held at 723.15 K at an oxygen ambience of 1.3×10^{-2} mbar. A series of three separate deposition processes were executed, with all deposition parameters held constant. The control of film thickness was achieved by adjusting the number of laser pulses employed for ablating YFO nanoparticles from the bulk YFO target. Specifically, three different film thicknesses were fabricated, corresponding to 7000, 9000, and 12,000 laser pulses. A detailed summary of the deposition parameters for the YFO thin films can be found in Table 1.

Table 1. Deposition parameters for the YFO thin films.

Sample	Fluency (Laser Energy Density)	Laser Pulses	Repetition Rate	Deposition Time (s)	Substrate Temperature	Gas Pressure (O₂)
YFO/Si-1 (S1)		12,000		2400		
YFO/Si-2 (S2)	2 J/cm^2	9000	5 Hz	1800	723.15 K	1.3×10^{-2} mbar
YFO/Si-3 (S3)		7000		1400		

Atomic force microscopy (AFM) was used to investigate the surface topography in contact mode using an NTegra Prima system (Spectrum Instruments, Zelenograd, Russia) and a CSG01 probe with a tip diameter of 6 nm. In contact mode, the AFM probe maintains continuous contact with the sample surface as it scans, allowing for high-resolution imaging. The interactions between the probe tip and the surface cause deflections in the flexible cantilever, which are detected by a laser beam reflected onto a position-sensitive photodetector. These deflections are converted into detailed topographical data, providing precise surface characterization at the nanoscale.

Ellipsometric measurements were carried out using a spectroscopic ellipsometer (J.A. Woollam Co., Inc., Lincoln, NE, United States, variable angle spectroscopic ellipsometer (VASE)). The instrument was equipped with a monochromatic light source capable of producing a broad spectrum of wavelengths (e.g., 190 nm to 1000 nm) and a rotating analyzer configuration. Measurements were taken at 60° and 80° angles of incidence. The angle range was chosen to ensure sufficient sensitivity to both the film thickness and optical properties. For each angle of incidence, the ellipsometric parameters Ψ (psi) and Δ (delta) were recorded across the selected wavelength range. Ψ represents the amplitude ratio, and Δ represents the phase difference between the p- and s-polarized light components upon reflection. The optical constants (refractive index, n, and extinction coefficient, k) were extracted by fitting the experimental data to the theoretical model using regression analysis. The fitting process was performed using the software provided with the ellipsometer (WVASE32).

X-ray photoelectron spectroscopy (XPS) measurements were conducted using an AXIS Supra XPS system (Kratos Analytical Ltd., Manchester, UK). This system is equipped with a monochromatic Al Kα X-ray source (1486.6 eV) and a hemispherical energy analyzer, providing high-resolution and high-sensitivity surface chemical analysis. Samples were mounted on the sample holder using conductive copper tape to ensure good electrical contact and minimize charging effects during measurement. The measurements were carried out in ultra-high vacuum conditions ($<10^{-9}$ mbar). The XPS spectra were acquired using the Al Kα X-ray source, operated at 150 W power (15 kV, 10 mA). Survey scans were performed over the binding energy range of 0 to 1200 eV to identify the elemental composition of the $YFeO_3$ films. High-resolution scans were acquired for the core-level regions of Y 3d, Fe 2p, and O 1s to obtain detailed chemical state information. The pass energy for survey and high-resolution scans was set to 80 eV and 20 eV, respectively. The acquired spectra were processed using the CasaXPS software (version 2.3.23, Kratos Analytical Ltd., Manchester, UK) using a Gaussian–Lorentzian model. Background subtraction was performed using the Shirley method to remove inelastic scattering contributions.

Raman spectroscopy measurements were performed using a WITec alpha300 R Raman microscope (WITec, Ulm, Germany). The system was equipped with a high-resolution CCD detector and a monochromatic laser source with an excitation wavelength of 532 nm. The laser power was set to 20 mW to ensure optimal signal intensity while avoiding sample damage. The Raman microscope was calibrated using a silicon standard to ensure the accuracy of the Raman shift measurements. The characteristic Si peak at 520.7 cm^{-1} was used for this calibration. The obtained Raman spectra were processed using WITec Project software. PL spectra were recorded using the same 355 nm laser excitation at 4 mW power. The spectral range for PL measurements was typically from 400 nm to 800 nm, depending on the expected emission wavelengths of the $YFeO_3$ films. There were 50 accumulations for Raman spectra and integration time was 10s. Similar to the Raman measurements, the PL signal was accumulated over 5 scans with an integration time of 25 s per scan to improve the signal-to-noise ratio and ensure reliable data. Fourier transform infrared (FTIR) spectroscopy was employed to investigate and confirm the structural properties of the YFO films. The FTIR spectra were recorded using a Vacuum FTIR Vertex70v spectrometer (Bruker), operated in reflectance mode. The measurements were conducted with a resolution of 4 cm^{-1}. The samples were placed in the vacuum

chamber of the spectrometer to avoid interference from atmospheric gases and moisture, ensuring higher accuracy in the measured spectra.

Reflectance measurements and band gap determination were performed using a JASCO V-670 UV–Vis–NIR spectrophotometer (JASCO International Co., Ltd., Tokyo, Japan). The instrument is equipped with a dual-grating monochromator, allowing high-resolution measurements across a broad spectral range from 190 nm to 2700 nm. The spectrophotometer was also configured with an integrating sphere attachment to accurately measure diffuse and specular reflectance. The spectrophotometer was calibrated using a certified reflectance standard (calibrated white standard). This step ensured the accuracy and reproducibility of the reflectance measurements. The reflectance data were processed using the JASCO Spectra Manager software (version 2.5). Baseline correction (using spectralon material) was applied to account for any instrumental background.

To evaluate the film adhesion and measure the film thickness, cross-sectional imaging was carried out using a Helios focused ion beam scanning electron microscope (FIB-SEM) (Thermo Fisher Scientific). Prior to cutting, a protective layer of tungsten (W) coating was deposited onto the film surface to prevent any potential damage during the milling process. The cross-sections were cut using an ion beam current of 2.5 nA to expose the underlying layers, followed by polishing with a finer current of 0.23 nA to produce a smoother surface for accurate imaging. This approach enabled high-resolution visualization of the film's interface with the substrate, ensuring reliable thickness measurements and a clear view of the adhesion quality between the layers. This high-resolution electron microscope provided detailed surface imaging, allowing the identification of fine structural features and ensuring an accurate assessment of surface uniformity. SEM imaging was essential for observing any surface irregularities or defects on the sample.

3. Results

The surface exhibited nonuniform topography, with variations in height up to 35 nm. The data are presented in Supplementary File S1 in a common format of scanning probe microscopy files. The presence of surface defects such as pits, cracks, or inclusions was identified (Figure 1). Comparisons of the samples shows that the roughness decreases with the growth of film, which covers the defects of the silicon substrates (the source of the surface inhomogeneities).
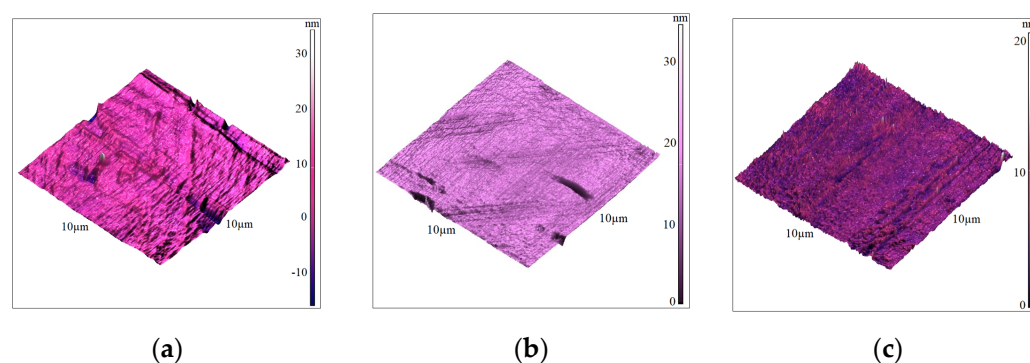

Figure 1. AFM images of the films surfaces of 10×10 μm. (**a**) S1; (**b**) S2; (**c**) S3.

The XPS spectra were calibrated using the C 1s peak at 284.6 eV as a reference to ensure accurate binding energy measurements. This contamination is commonly observed in XPS measurements due to exposure to air. If necessary, the carbon contamination can be reduced or eliminated by annealing the samples in a high-vacuum environment. The survey spectra, as shown in Figure 2, confirm the presence of iron (Fe), yttrium (Y), and oxygen (O) in the $YFeO_3$ films. The identification of these elements is consistent with the expected stoichiometry of the $YFeO_3$ compound. The detailed spectra of each element are presented
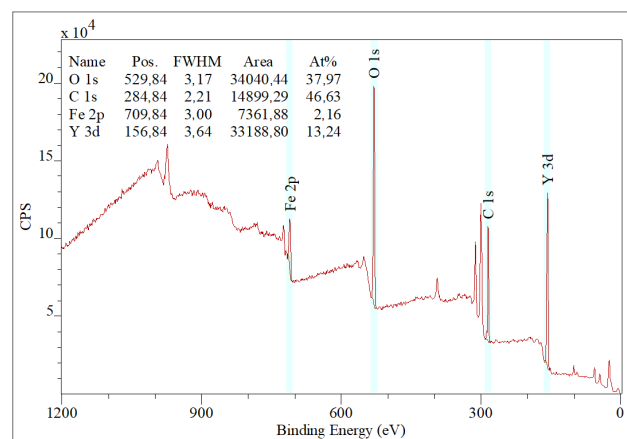
in Figure 3 with the binding energy plotted along the *X*-axis and the corresponding counts per second (CPS) represented on the *Y*-axis.
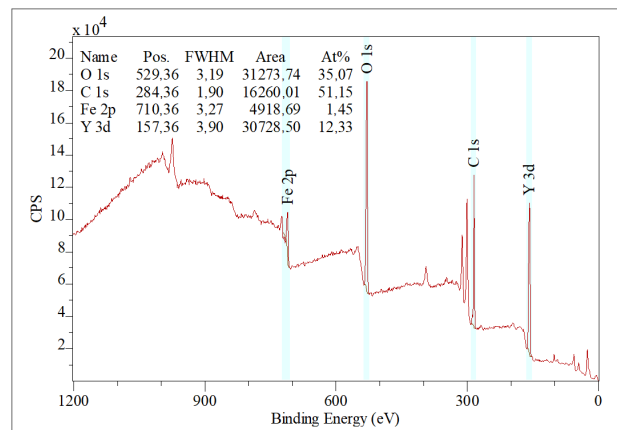
(a)
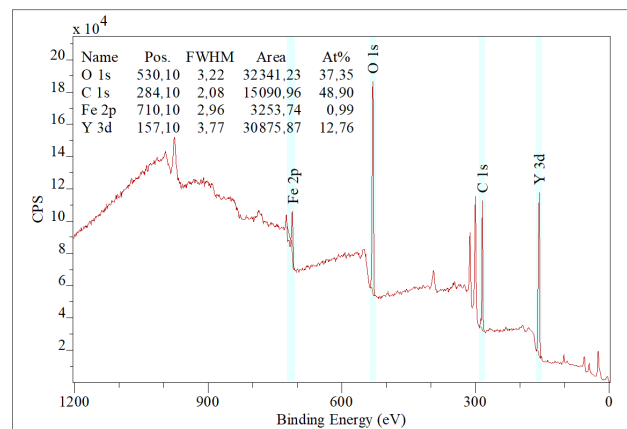
(b)

(c)

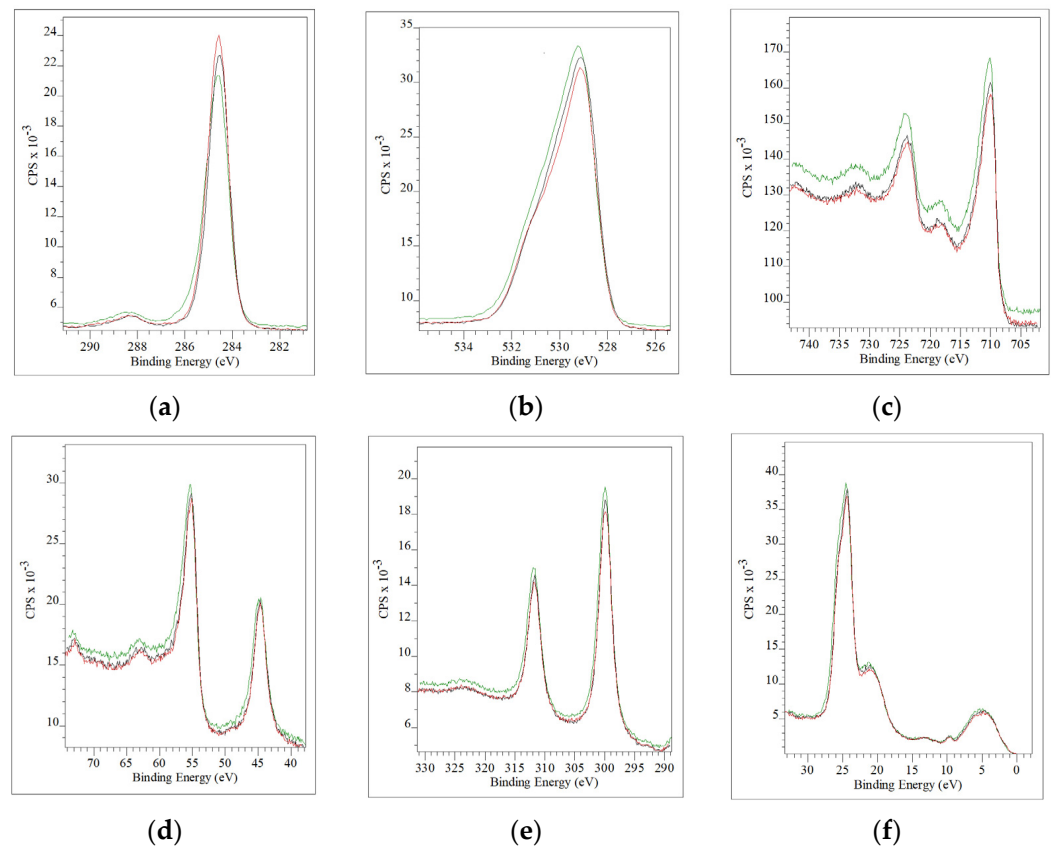**Figure 2.** XPS Survey spectra of the films. (**a**) S1; (**b**) S2; (**c**) S3.

Figure 3. XPS detailed spectra of the films (red—S1, black—S2, green—S3): (**a**) C1s; (**b**) O1s; (**c**) Fe2p; (**d**) Fe3p; (**e**) Y3p; (**f**) VB.

The high-magnification (100×) objective enabled precise focusing and collection of Raman signals from specific areas of the film, enhancing the detection of subtle structural features (Figure 4b). To visually assess the homogeneity of the YFeO$_3$ films, an optical image of the sample was taken using a lower-magnification objective lens, as shown in Figure 4a. This image provides an overview of a larger area of the film, highlighting its uniformity and consistency in real colors. The lower-magnification image ensures that any macroscopic inhomogeneities or defects are clearly visible, thus supporting the comprehensive analysis of film quality.
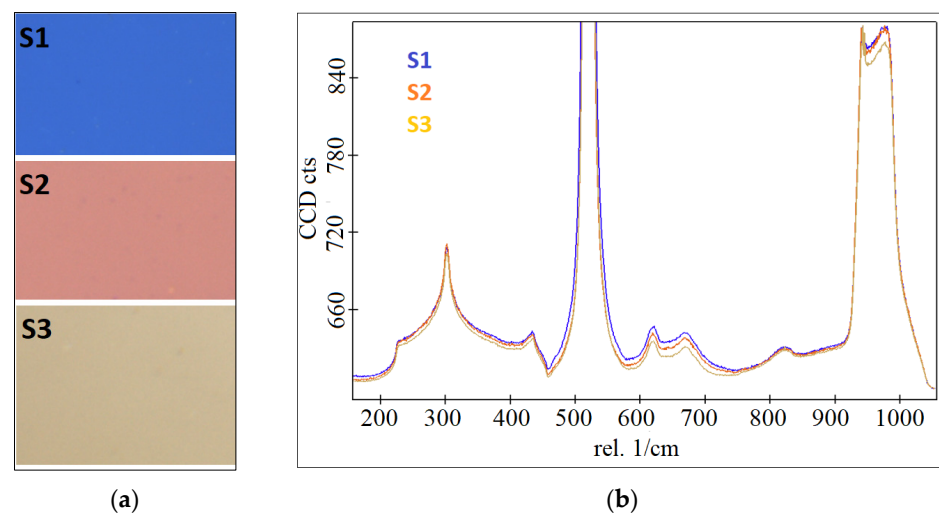
Figure 4. Optical image of the films with magnification 50× (**a**) and Raman spectra (**b**).

To demonstrate the homogeneity of the films the scanning electron microscopy and cross-section imaging are provided below (Figure 5).
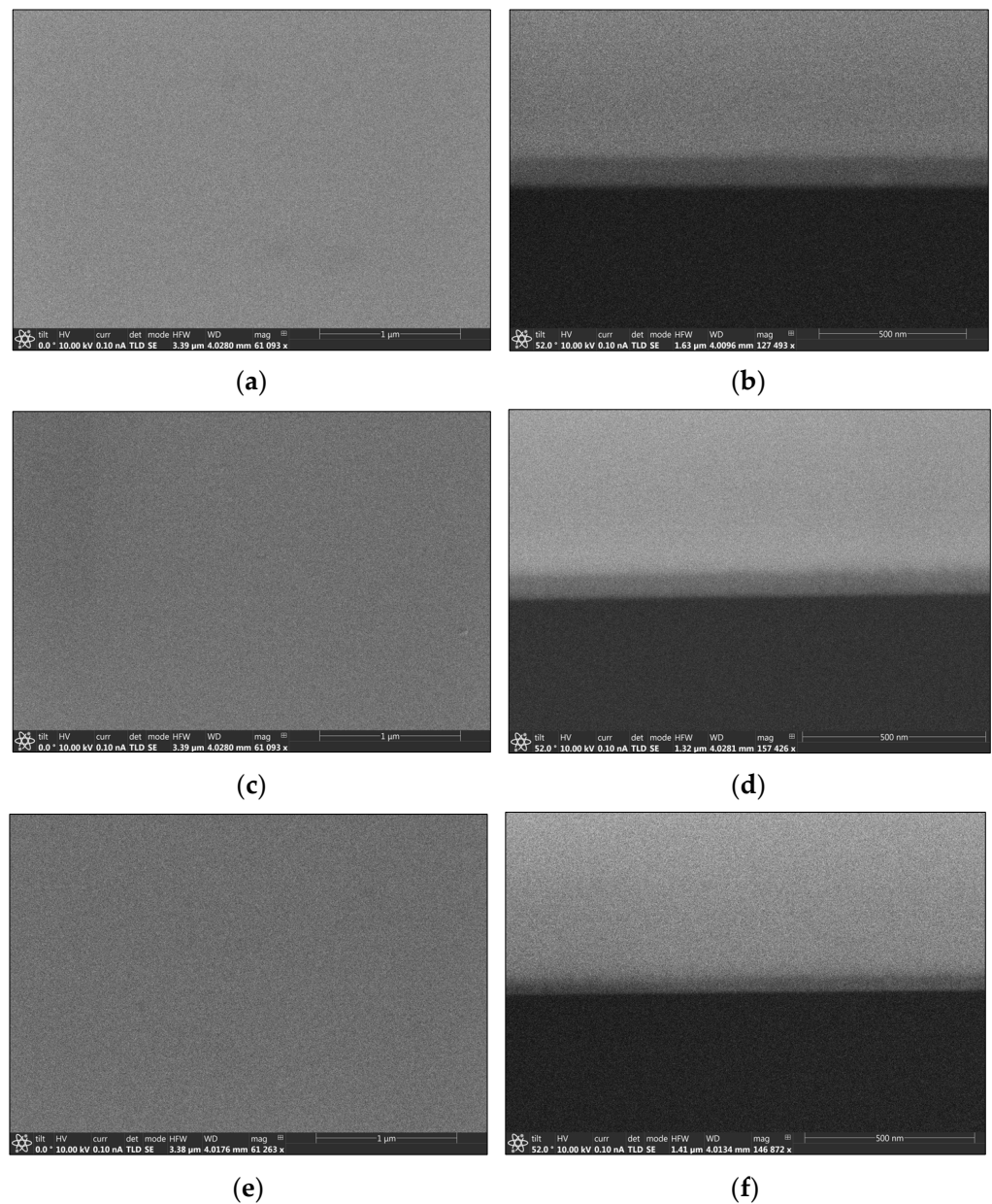
(a)

(b)

(c)

(d)

(e)

(f)

Figure 5. SEM images of S1 (**a**), S2 (**c**), and S3 (**e**) samples and cross-sections of the samples with thickness 93 nm—S1 (**b**), 66 nm—S2 (**d**), and 44 nm—S3 (**f**).

FTIR plays a crucial role in providing insights into both the vibrational and optical properties of the material. FTIR reflectance spectra displayed several characteristic peaks that confirm the formation of the YFO phase and its associated vibrational structures (Figure 6).

The PL spectra were acquired using a UV laser with a 40x magnification objective lens, which provided a balance between spatial resolution and area coverage, ensuring detailed yet comprehensive analysis of the film's luminescent properties. To enhance the clarity and readability of the PL spectra, the raw data were processed using an averaging filter. This smoothing process helped to reduce noise and improve the signal-to-noise ratio, resulting in clearer and more interpretable spectral features (Figure 7).
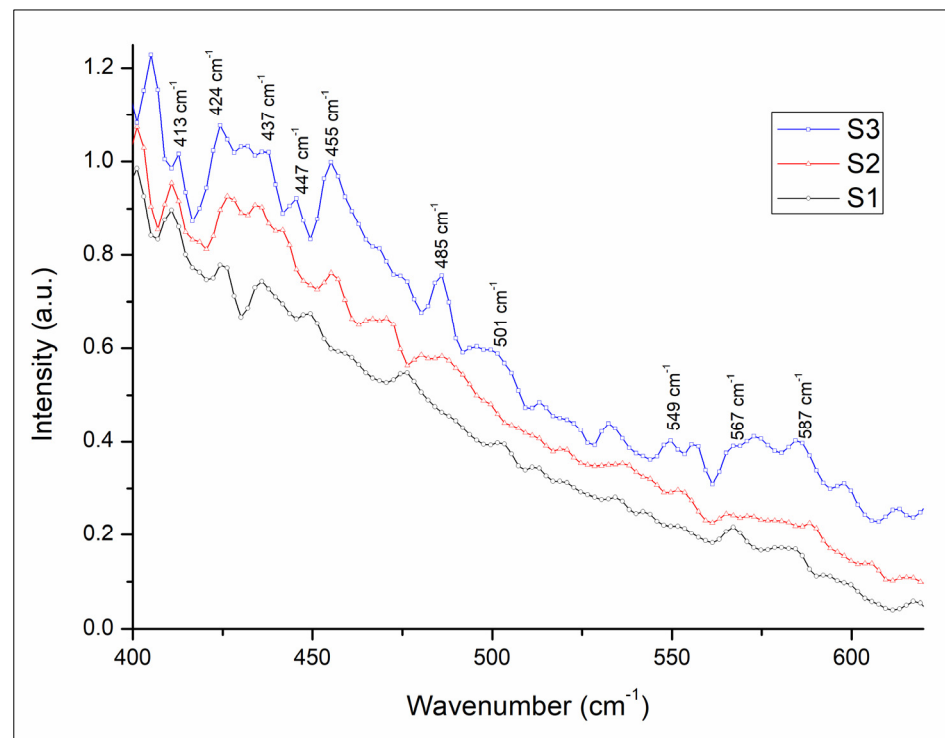
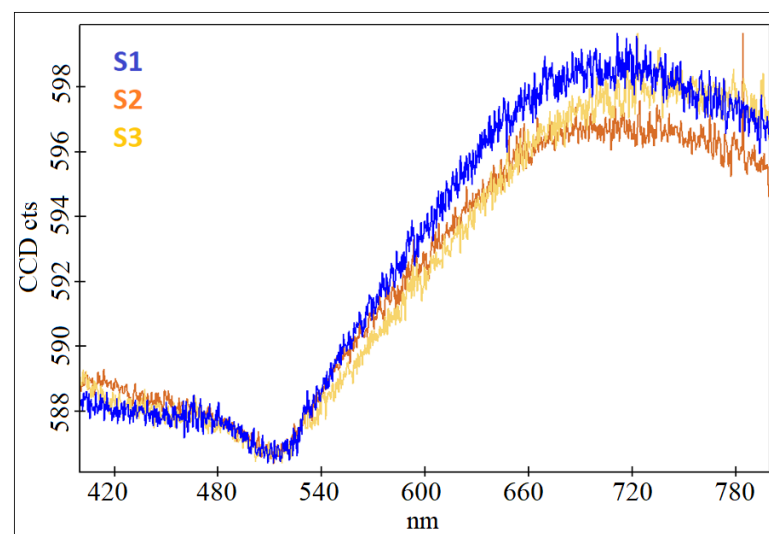**Figure 6.** FTIR reflectance spectra of S1, S2, and S3 samples.

**Figure 7.** Photoluminescence measurement of the YFO films.

Ellipsometry provided detailed insights into the optical properties of the $YFeO_3$ films, revealing key parameters such as the refractive index, extinction coefficient, and dielectric functions. These optical properties were found to have a significant correlation with the electrical performance of the films. The analysis demonstrated that regions with higher refractive indices and dielectric functions corresponded to improved electrical conductivity and mobility (Figures 8 and 9).
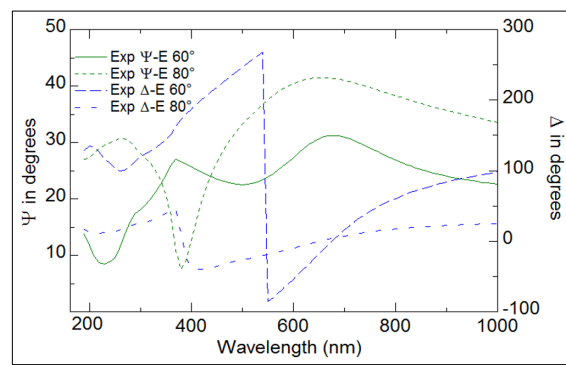
(a)
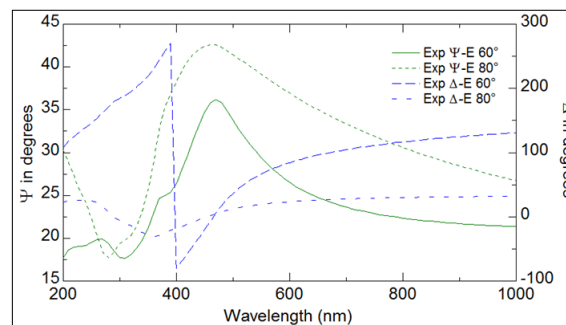
(b)
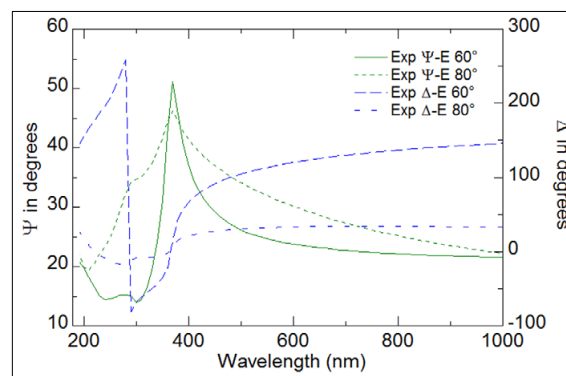
(c)

Figure 8. Ellipsometry spectra of the films. (**a**) S1; (**b**) S2; (**c**) S3.

Reflectance measurements were conducted to determine the optical band gap, Urbach energy, and the nature of electronic transitions (direct/indirect and allowed/forbidden) in the YFO films. These optical parameters provide crucial insights into the electronic structure and optical properties of the material. The optical band gap is determined using Tauc plots derived from the reflectance data. The absorption coefficient was calculated using the Kubelka–Munk function. Detailed calculation is given in Supplementary Material S5 (Figure 10).
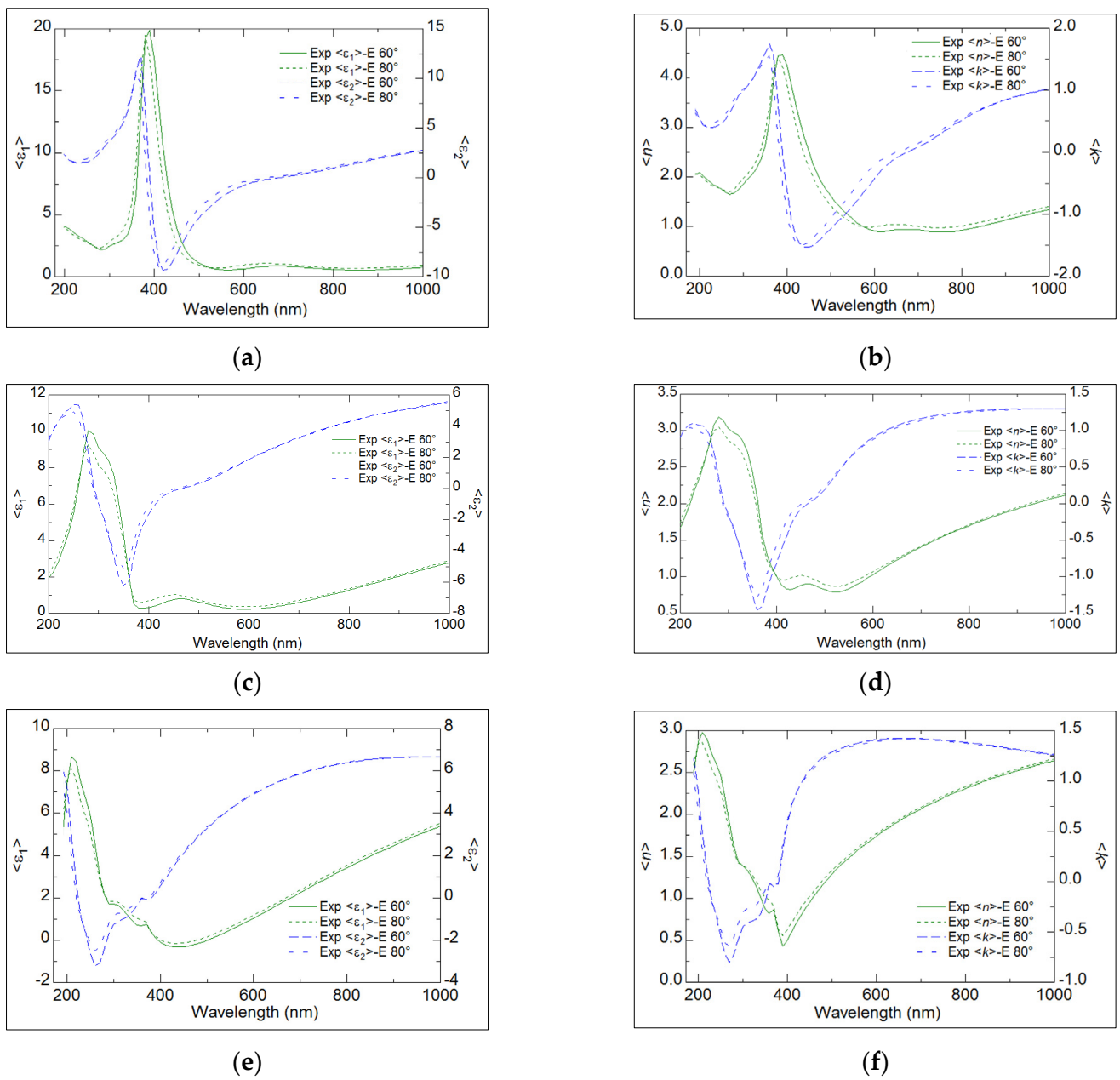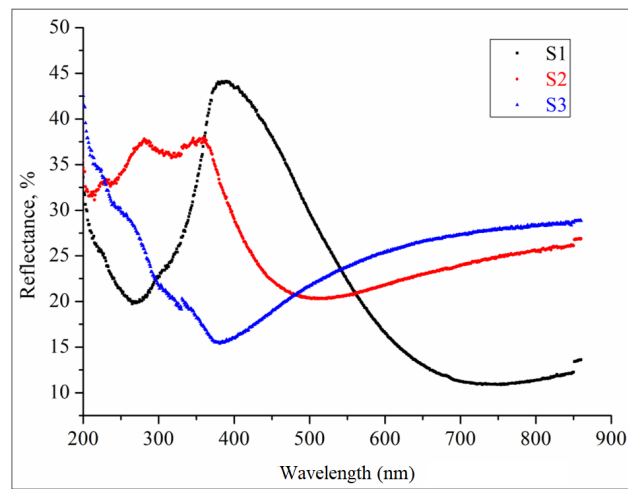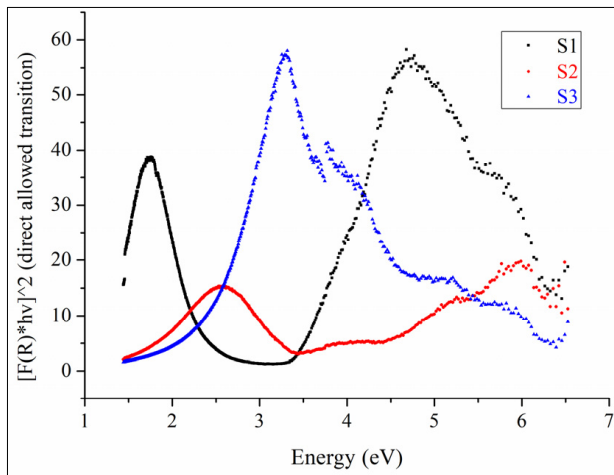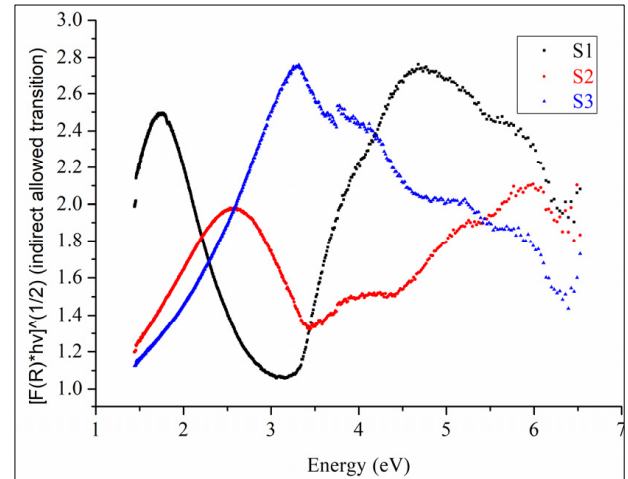
Figure 9. Optical and electrical characteristics recalculated from ellipsometry spectra of the films. (**a**,**b**) S1; (**c**,**d**) S2; (**e**,**f**) S3.
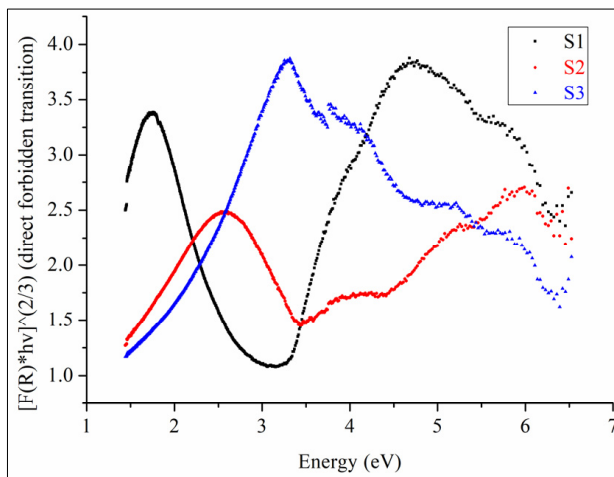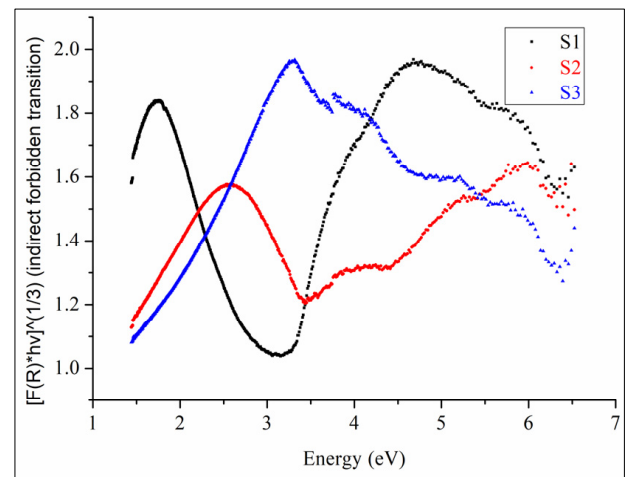
Figure 10. Reflectance of the films: (**a**), direct allowed transitions (**b**), indirect allowed transition (**c**), and forbidden transitions (**d**,**e**).

4. Discussion

The analysis of the YFO films revealed several key insights regarding their morphology, elemental composition, and electronic structure. The smoothest morphology was observed for the film labeled S3, which effectively covered the defects present on the silicon substrates. This indicates that the deposition process for S3 resulted in a more uniform and defect-free film surface, enhancing its overall quality and potential performance in applications requiring smooth, continuous films (Figure 1 and Supplementary Material S1). The XPS wide spectra provided valuable information about the elemental composition of the films. The data showed that the amount of yttrium increased with the number of deposition pulses, indicating successful incorporation of yttrium into the film structure as deposition progressed. A slight increase in the oxygen O1s peak was also observed, consistent with the formation of YFO, which requires oxygen for its stoichiometric balance. Given the surface sensitivity of XPS, a significant C1s peak was detected (Figure 2). However, this peak is attributed to adventitious carbon contamination from the environment and is not part of the intrinsic film structure. Notably, the S1 sample exhibited a lower carbon content, likely due to its smoother and less developed morphology, which reduces surface area available for contamination. The Fe 2p peak intensity was higher for the S3 film, and this was corroborated by additional Fe 3p scans. The Y 3p signal was more pronounced, further confirming the increased presence of these elements in the S3 film (Figure 3). The observation that the valence band position is unchanged implies that the differences in the electronic structure among the samples are due to variations in the conduction band position and defect states within the band gap. These findings are crucial for understanding the electronic behavior of the films and for optimizing their properties for specific applications, such as optoelectronics or photovoltaics (Supplementary Material S2). The FIB-SEM cross-sectional analysis revealed that the deposited films exhibit excellent adhesion to the substrate, with no evidence of voids, inclusions, or delamination at the interface. This strong adhesion is critical for ensuring the durability and performance of the films in their intended applications. The thickness of the films was consistent with expectations, correlating directly with the number of deposition pulses applied during the process. As anticipated, increasing the number of pulses led to a proportional increase in film thickness. Furthermore, the SEM surface analysis demonstrated that the films possess a high degree of homogeneity, with a smooth and uniform surface morphology. The absence of irregularities or defects on the surface indicates that the deposition process was well-controlled, contributing to the overall quality of the films. This uniformity and smoothness are essential for the films' functionality, particularly in applications requiring precision and consistency in material properties.

The optical photographs of the films reveal their real colors, indicating that the optical properties of the films are indeed influenced by the number of deposition pulses, which in turn correlates with film thickness. As the number of pulses increases, the films become thicker, leading to changes in their color and optical behavior. This relationship highlights the importance of controlling deposition parameters to tailor the optical properties of the films for specific applications. The Raman spectroscopy results did not prominently show the presence of the YFO films due to the laser's penetration depth being greater than the film thickness. Consequently, the spectra were dominated by a very intense peak from the silicon substrate, which matched perfectly with the characteristic Raman signal of silicon. The YFO Raman fingerprints were very weak and not clearly observable. However, for the S1 sample, which is supposed to be thicker, there was a slight shading of the silicon signal, suggesting that the thicker film partially attenuated the substrate's Raman signal. This observation confirms that the film thickness affects the detectability of the film's Raman signal, with thicker films offering better coverage and potentially more pronounced signals (Figure 4).

The FTIR spectral region around 567 cm^{-1} stands out as particularly significant due to its direct association with the vibrational mode of octahedral FeO_6 units (Figure 6). This vibrational signature serves as a key indicator of the structural characteristics of the

material, providing strong evidence that supports the successful formation of a pure $YFeO_3$ phase. As reported by Ahmad et al. (2017) [18], the presence of this specific vibration is a distinctive hallmark of the $YFeO_3$ structure, and its clear observation in our measurements further confirms the integrity of the synthesized phase. Other notable features appear within the spectral range between 425 and 555 cm^{-1}, which include a prominent band at 552 cm^{-1}. This band, as observed in perovskite-based materials, is linked to the stretching vibrations of metal–oxygen bonds, specifically Fe–O, which are fundamental to the perovskite framework. The identification of these peaks is critical for determining not only the phase of the material but also the precise bonding configuration [11]. Moreover, several intense bands were detected in the 600 to 400 cm^{-1} region, which are indicative of vibrational bending within the metal–oxygen bonds in the dodecahedral units commonly found in garnet structures. Particularly, peaks at 575 cm^{-1} and 463 cm^{-1} have been identified as attributable to Fe–O bond interactions. According to Vázquez-Olmos et al. (2018) [14], these bands provide further evidence of the complex bonding environment within the material and contribute to understanding its overall vibrational behavior. FTIR spectra reveal two distinct bands around 587 cm^{-1}, which are closely associated with the stretching vibrations of Fe–O bonds. These bands, characteristic of the octahedral FeO_6 groups, are often found in perovskite structures and have been widely documented in the literature. The work of Gil et al. (2011) [19] confirms that such bands are indicative of the octahedral coordination within the perovskite lattice, thereby offering further confirmation of the phase purity and structural coherence of the YFO films analyzed in this study.

The PL spectra provided additional insights into the optical properties of the films. The S1 sample exhibited higher PL intensity, which can be attributed to unresolved mechanical stress within the film. This stress can lead to an increase in PL emission, indicating that the mechanical properties of the films significantly influence their optical behavior. The higher PL intensity in the S1 sample suggests that the YFO films are under mechanical stress which increased with film thickness (Figure 7, Supplementary S3).

The results from the ellipsometry measurements indicated that the maxima of both ε' (real part of the dielectric function) and ε'' (imaginary part of the dielectric function) shifted to lower wavelengths as the number of pulses used for film preparation increased. This trend suggests that the optical properties of the films are strongly influenced by their thickness, with thinner films showing a blue shift in the dielectric function peaks. Interestingly, the highest value of ε' was observed for the sample S1. This indicates that the S1 sample has a higher ability to store electrical energy, being thicker than the other samples. The refractive index and the extinction coefficient also showed similar trends to those observed for ε' and ε''. The maxima of n and k moved to lower wavelengths with an increasing number of deposition pulses. This behavior suggests a systematic change in the optical density and absorption characteristics of the films as they become thicker. The highest values of n and k were observed for the S1 sample, similar to the dielectric function, which highlights the unique optical properties of the S1 sample compared to thinner films. Ellipsometry measurements were conducted at two different angles of incidence, 60° and 80°, to ensure the reliability of the data. The trends observed for ε', ε''', n, and k at both angles were consistent, confirming the robustness and reliability of the ellipsometric analysis (Figures 8 and 9, Supplementary Material S4).

Figure 10 demonstrates the reflectance of the samples (Supplementary Material S5), where the minimum moves to the shorter wavelength with growth of the pulses for the film's preparation. The reflectance data were used to show the spectra which helps to describe the conduction band. The theory behind this was previously reported by a number of works and is summarized in Figure 11. The findings align with previous works, as the characterization of electronic transitions through reflectance measurements supports the presence of distinct energy levels associated with both allowed and forbidden transitions [20]. The observed band gap energy changes are consistent with reported strain-induced band gap tuning [21]. The previous results indicated that the band gap can increase with decreasing film thickness due to quantum confinement effects. This effect is

attributed to changes in the electronic structure as the film transitions from a bulk-like state to a two-dimensional state. The observed allowed direct and indirect transitions align with the theoretical predictions of Singh N. et al. [22] dedicated to calculated band structure. The direct and indirect allowed transitions calculated from reflectance are observed to shift to higher energies with the decreasing of the film thickness, which typically indicates changes in the electronic and optical properties of the material as the film becomes thicker. The growth of the film can introduce strain and stress within the material. Thin films often experience different stress states compared to bulk materials. The change in strain with increasing thickness can affect the electronic band structure of the material, leading to shifts in transition energies. Forbidden transitions in materials are electronic transitions that are theoretically disallowed by certain selection rules in quantum mechanics [23,24].
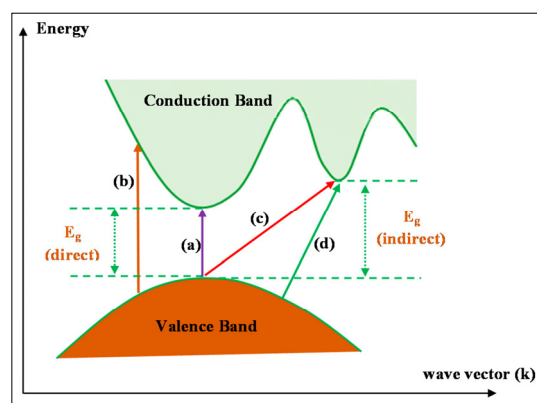

Figure 11. Electronic transitions: (a) allowed direct, (b) forbidden direct, (c) allowed indirect, and (d) forbidden indirect [25].

However, these transitions can still occur, albeit with lower probability compared to allowed transitions. The theoretically forbidden transitions can still happen because we report heteroepitaxial growth, where the break of the symmetry between the substrate and the film occurs, proved by PL data. In addition, phonon interactions also perturb the electron states, enabling forbidden transitions by providing the additional energy or momentum required to satisfy the conservation laws.

5. Conclusions

In conclusion, the film deposited with the highest number of pulses demonstrated the smoothest morphology, improved elemental incorporation, and consistent valence band positioning, making it the most promising candidate among the samples studied. The higher PL intensity in the S1 sample points to the impact of mechanical stress on luminescence properties. This stress-induced PL enhancement implies that stress management during film deposition is crucial for achieving desired optical characteristics. The ellipsometry analysis reveals that the optical properties of the YFO films, including the dielectric function, refractive index, and extinction coefficient, are significantly influenced by the film thickness, which is controlled by the number of deposition pulses. The shift of the maxima to lower wavelengths with increasing film thickness and the highest values observed for the S1 sample indicate distinct optical characteristics for thinner films. The consistency of the results across different angles of incidence further supports the reliability of the data. The shift of direct allowed transitions to higher energies with increasing film thickness suggests that the optical and electronic properties of the material are evolving with thickness. This may be due to a combination of quantum confinement, strain effects, surface and interface influences, changes in material quality, and optical interference. Similar to allowed transitions, forbidden transitions also shift in energy with changes in film thickness. This may happen due to alterations in the electronic band structure, strain effects,

quantum confinement, and other factors. These findings provide valuable insights into the optical behavior of YFO films and their potential applications in optoelectronic devices.

References

1. Stoeffler, D.; Chaker, Z. First Principles Study of the Electronic Structure and Magnetic Properties of $YFeO_3$ Oxide. *J. Magn. Magn. Mater.* **2017**, *442*, 255–264. [CrossRef]
2. Dedov, G.S.; Shorikov, A.O. Theoretical Study of the Epitaxial Strain Effect on the Structural and Magnetic Properties of a $YFeO_3$ Thin Film on a $SrTiO_3$ Substrate. *JETP Lett.* **2024**, *119*, 696–702. [CrossRef]
3. Shang, M.; Zhang, C.; Zhang, T.; Yuan, L.; Ge, L.; Yuan, H.; Feng, S. The Multiferroic Perovskite $YFeO_3$. *Appl. Phys. Lett.* **2013**, *102*, 62903. [CrossRef]
4. Wang, Z.; Zhao, W.; Li, Z.; Peng, Y.; Gao, C.; Shi, L.; Hua, W.; Fei, W.; Zhao, Y. Multiferroic Properties of Ba2+-Ti4+ Co-Doped $YFeO_3$ Ceramics. *J. Alloys Compd.* **2023**, *960*, 170718. [CrossRef]
5. Sharon, M.; Prasad, B.M. Preparation and Photocharacterization of $YFeO_3$ Semiconductor. *Electrochim. Acta* **1985**, *30*, 331–334. [CrossRef]
6. Ismael, M.; Elhaddad, E.; Taffa, D.H.; Wark, M. Synthesis of Phase Pure Hexagonal $YFeO_3$ Perovskite as Efficient Visible Light Active Photocatalyst. *Catalysts* **2017**, *7*, 326. [CrossRef]
7. Sasmal, A.; Sen, S.; Chelvane, J.A.; Arockiarajan, A. PVDF Based Flexible Magnetoelectric Composites for Capacitive Energy Storage, Hybrid Mechanical Energy Harvesting and Self-Powered Magnetic Field Detection. *Polymer* **2023**, *281*, 126141. [CrossRef]
8. Wang, M.; Wang, T.; Song, S.; Tan, M. Structure-Controllable Synthesis of Multiferroic $YFeO_3$ Nanopowders and Their Optical and Magnetic Properties. *Materials* **2017**, *10*, 626. [CrossRef]
9. Sui, Y.; Lu, F.; Liu, X.; Zhang, Y.; Sun, X.; Liu, C. A Novel Hexagonal $YFeO_3$ 3D Nanomaterial with Room Temperature Ferromagnetic Properties Prepared by Self-Assembling Method. *Results Mater.* **2021**, *10*, 100186. [CrossRef]
10. Chung, N.T.K.; Tien, N.A.; Vuong, B.X. Optical and Magnetic Properties of $YFeO_3$ Nanoparticles Synthesized by a Co-Precipitation Method at High Temperature. *Chem. Pap.* **2022**, *76*, 923–930. [CrossRef]
11. Suthar, L.; Bhadala, F.; Roy, M. Structural, Electrical, Thermal and Optical Properties of $YFeO_3$, Prepared by SSR and Sol–Gel Route: A Comparative Study. *Appl. Phys. A Mater. Sci. Process* **2019**, *125*, 452. [CrossRef]
12. Jiang, J.; Dai, Y.; Shang, J.; Zhang, Z.; Su, L.; Cheng, M.; Sun, D.; Stupakiewicz, A.; Wu, A. Perpendicular Magnetic Anisotropy and Magneto-Optical Properties of Bi,Mn:YIG Epitaxial Films. *CrystEngComm* **2023**, *26*, 32–39. [CrossRef]
13. Rosales-González, O.; Sánchez-De Jesús, F.; Cortés-Escobedo, C.A.; Bolarín-Miró, A.M. Crystal Structure and Multiferroic Behavior of Perovskite $YFeO_3$. *Ceram. Int.* **2018**, *44*, 15298–15303. [CrossRef]
14. Vázquez-Olmos, A.R.; Sánchez-Vergara, M.E.; Fernández-Osorio, A.L.; Hernández-García, A.; Sato-Berrú, R.Y.; Alvarez-Bada, J.R. Mechanochemical Synthesis of $YFeO_3$ Nanoparticles: Optical and Electrical Properties of Thin Films. *J. Clust. Sci.* **2018**, *29*, 225–233. [CrossRef]
15. Baqiah, H.; Awang Kechik, M.M.; Al-Gaashani, R.; Al-Zahrani, A.A.; Al-Hada, N.M.; Zhang, N.; Liu, J.; Xu, S. Effects of Annealing Temperature on the Phase Formation, Optical, Photoluminescence and Magnetic Properties of Sol-Gel $YFeO_3$ Films. *Ceram. Int.* **2023**, *49*, 600–606. [CrossRef]
16. Phan Vu, T.V.; Nguyen, M.T.; Nguyen, D.T.T.; Vu, T.D.; Nguyen, D.L.; An, N.M.; Nguyen, M.H.; Sai, C.D.; Bui, V.D.; Hoang, C.H.; et al. Three-Photon Absorption Induced Photoluminescence in Organo-Lead Mixed Halide Perovskites. *J. Electron. Mater.* **2017**, *46*, 3622–3626. [CrossRef]

17. Apostolov, A.; Apostolova, I.; Wesselinowa, J. Multiferroic, Phonon and Optical Properties of Pure and Ion-Doped $YFeO_3$ Nanoparticles. *Nanomaterials* **2021**, *11*, 2731. [CrossRef]

18. Ahmad, T.; Lone, I.H.; Ansari, S.G.; Ahmed, J.; Ahamad, T.; Alshehri, S.M. Multifunctional Properties and Applications of Yttrium Ferrite Nanoparticles Prepared by Citrate Precursor Route. *Mater. Des.* **2017**, *126*, 331–338. [CrossRef]

19. Gil, D.M.; Navarro, M.C.; Lagarrigue, M.C.; Guimpel, J.; Carbonio, R.E.; Gómez, M.I. Synthesis and Structural Characterization of Perovskite $YFeO_3$ by Thermal Decomposition of a Cyano Complex Precursor, $Y[Fe(CN)_6] \bullet 4H_2O$. *J. Therm. Anal. Calorim.* **2011**, *103*, 889–896. [CrossRef]

20. Warshi, M.K.; Kumar, A.; Mishra, V.; Sati, A.; Sagdeo, A.; Kumar, R.; Sagdeo, P.R. Effect of Self-Doping on the Charge State of Fe Ions and Crystal Field Transitions in $YFeO_3$: Experiments and Theory. *J. Appl. Phys.* **2019**, *125*, 204101. [CrossRef]

21. Sun, Y.; Wong, K.H.; Kwok, K.W. Strain-Induced Band Gap Tuning in Flexible Ferroelectric/Mica Thin Films. *Thin Solid Film.* **2021**, *731*, 138741. [CrossRef]

22. Singh, N.; Rhee, J.Y.; Auluck, S. Electronic and Magneto-Optical Properties of Rare-Earth Orthoferrites $RFeO_3$ (R = Y, Sm, Eu, Gd and Lu). *J. Korean Phys. Soc.* **2008**, *53*, 806–811. [CrossRef]

23. Tarun, A.; Hayazawa, N.; Ishitobi, H.; Kawata, S.; Reiche, M.; Moutanabbir, O. Mapping the "Forbidden" Transverse-Optical Phonon in Single Strained Silicon (100) Nanowire. *Nano Lett.* **2011**, *11*, 4780–4788. [CrossRef] [PubMed]

24. Woods-Robinson, R.; Xiong, Y.; Shen, J.X.; Winner, N.; Horton, M.K.; Asta, M.; Ganose, A.M.; Hautier, G.; Persson, K.A. Designing Transparent Conductors Using Forbidden Optical Transitions. *Matter* **2023**, *6*, 3021–3039. [CrossRef]

25. Nofal, M.M.; Aziz, S.B.; Hadi, J.M.; Karim, W.O.; Dannoun, E.M.A.; Hussein, A.M.; Hussen, S.A. Polymer Composites with 0.98 Transparencies and Small Optical Energy Band Gap Using a Promising Green Methodology: Structural and Optical Properties. *Polymers* **2021**, *13*, 1648. [CrossRef]